

# Radar sounding of subsurface water-ice in eastern Coprates and Capri Chasmata, Mars

R. Noguchi<sup>1</sup>, K. Ishiyama<sup>1,2</sup>, A. Kumamoto<sup>3</sup>, C. Uemura<sup>4</sup>, Y. Kasaba<sup>3</sup>, T.  
Usui<sup>1,5</sup>, A. Oura<sup>3</sup>, and D. Shoji<sup>5</sup>

<sup>1</sup>Institute of Space and Astronautical Science, Japan Astronautical Exploration Agency, 3-1-1 Yoshinodai,  
252-5210, Sagami-hara, Kanagawa, Japan

<sup>2</sup>National Institute of Technology, Tsuruoka College, 104 Sawada, Inooka, Tsuruoka, Yamagata 997-8511,  
Japan

<sup>3</sup>Tohoku University, Aramaki-Aza-Aoba 6-3, Aoba-ku, Sendai, Miyagi, 980-8578, Japan

<sup>4</sup>SOKENDAI (Graduate University for Advanced Studies), 3-1-1 Yoshinodai, Sagami-hara, Kanagawa,  
252-5210, Japan

<sup>5</sup>Earth-Life Science Institute, Tokyo Institute of Technology, 2-12-1 Ookayama, Meguro, Tokyo, 152-8550,  
Japan

## Key Points:

- We identified subsurface reflectors in four areas in the eastern Coprates and Capri Chasmata based on SHARAD data.
- Dielectric constants estimated using HiRISE data provide the upper limit of the possible volume fraction of water-ice as 21.2 %.
- This upper limit yields the maximum volume of putative subsurface water-ice in the chasmata of 16.6 km<sup>3</sup>.

---

Corresponding author: Rina Noguchi, [r-noguchi@planeta.sci.isas.jaxa.jp](mailto:r-noguchi@planeta.sci.isas.jaxa.jp)

Corresponding author: Tomohiro Usui, [usui.tomohiro@jaxa.jp](mailto:usui.tomohiro@jaxa.jp)

**Abstract**

We surveyed the subsurface structure in eastern Coprates and Capri Chasmata in the equatorial region using high-resolution visible images, digital terrain models, and radar sounding data. We identified subsurface reflectors in four areas of the chasmata. At the stratigraphic exposure on the chasmata walls, the corresponding depth of the reflector is  $\sim 60$  m. The bulk dielectric constants of the layers above the reflectors are calculated as 3.4–4.0, suggesting a rock-air mixture with  $\sim 46.1\%$  porosity, or a rock-air-ice mixture with  $\sim 21.2\%$  water-ice fraction. Recent climate models suggest that water-ice is unstable on the surface around the equatorial regions. However, considering the recent high obliquity that occurred  $\sim 0.4$  Ma and a slow diffusivity of water-ice, the existence of subsurface water-ice deeper than a few meters cannot be ruled out. If water-ice is actually contained in the layer, our results show the maximum volume of putative water-ice in the chasmata is  $16.6 \text{ km}^3$ .

**1 Introduction**

While the effect of water on the Martian climate and geological evolution is important, the distribution of subsurface water/ice is not well known. Among the remote sensing methods, the radar sounding technique has the most potential to visualize the subsurface structure of Mars. This technique has revealed subsurface icy layering (*Putzig et al., 2018*) and possible subglacial liquid water beneath the polar caps (*Orosei et al., 2018*). A recent encompassing and amalgamating survey with other datasets has revealed the extent of the cryosphere using radar sounding data (*Bramson et al., 2015; Morgan et al., 2019; Stuurman et al., 2017*). For example, *Bramson et al. (2015)* estimated the existence of excess ice (higher water-ice abundances than the maximum porosity of dry regolith) due to low dielectric constants estimated by compiling exposed crater terraces and the subsurface radar reflectance. Thus, compiling various remote sensing data including the radar sounding technique will unveil the water-ice beneath the surface of Mars.

Interestingly, in contrast to the climate models that imply the ice is unstable, the existence of subsurface water-ice on current Mars at mid-latitudes has been indicated/suggested by several previous studies based on remote sensing observations (*Bramson et al., 2015; Byrne et al., 2009; Dundas et al., 2014; Stuurman et al., 2017*). From current Martian climate conditions, the existence of subsurface water-ice is not expected (e.g., *Schorghofer and Aharonson, 2005*). One piece of evidence for the existence of subsurface water-ice at the current mid-latitudes is the ice excavated by newly formed impact craters (*Byrne et al., 2009; Dundas et al., 2014*). The radar sounding technique has found possible subsurface extents of water-ice in mid-latitude planitiae (*Bramson et al., 2015; Stuurman et al., 2017*). Analyzing morphometry of expanded secondary craters, *Viola et al. (2015)* estimated that possible subsurface water-ice in Arcadia Planitia has been preserved for tens of millions of years. Thus, in the mid-latitude area, it seems that water-ice is preserved for a longer time than suggested by climate modeling evaluations.

On the other hand, at low-latitudes, current water-ice in the shallow subsurface has not been observed explicitly, although remnants of mountain glaciers have been found (*Head and Marchant, 2003; Milkovich et al., 2006*). Here, to survey the subsurface structure in the equatorial region, we compile visible images, topographic data, and radar sounding data at one of the largest outcrops on Mars: Valles Marineris. Valles Marineris has been characterized by water-related geologic features such as a distribution of a variety of aqueous minerals (e.g., sulfates *Chojnacki and Hynak, 2008*) and fluvial topography (*Carr and Head, 2010*, and references therein). Furthermore, swarms of recurring slope lineae (RSLs) possibly induced by water-related recurrent surface activity have been investigated (*Chojnacki et al., 2016; Stillman et*

72 *al.*, 2017), although the formation mechanisms are still under debate (e.g., *Dundas et*  
 73 *al.*, 2017). Thanks to those water-related features, dense and high-resolution remote  
 74 sensing datasets have been developed. Subsurface radar reflectors exist in several  
 75 areas of the Valles Marineris plateau (*Smith et al.*, 2019). Large and clear stratigra-  
 76 phy exposed on the walls could be assigned to those subsurface radar reflectors. A  
 77 flat and lightly cratered surface in the plateau of eastern Coprates and Capri Chas-  
 78 mata, the eastern portion of Valles Marineris, provides a reliable dataset for radar  
 79 sounding analysis, since rough surface topography causes artificial reflectors such as  
 80 surface clutter echos (*Seu et al.*, 2004). In this context, we selected eastern Coprates  
 81 and Capri Chasmata as targets of this compiling study.

## 82 2 Method

83 *Beyer and McEwen* (2005) described the stratigraphy of eastern Coprates and  
 84 northern Capri Chasmata in detail using visible images, infrared images, spectrum  
 85 data, and topographic data. There are exposed alternating thin strong layers and  
 86 thicker sequences of relatively weak layers (*Beyer and McEwen*, 2005). The top-  
 87 most strong layer is a 10 m-thick dark-toned layer and is thought to be a Hesperian  
 88 basaltic lava flow (*Witbeck et al.*, 1991). The sequences of relatively weak layers have  
 89 been indicated as sequences of thin flows interbedded with tephra or other sediments  
 90 (*Beyer and McEwen*, 2005).

91 At the point of interest, we described the exposed stratigraphy of the chasma  
 92 wall using visible images and topographic data (Fig.3B). Firstly, layers on outcrops  
 93 that are not covered with talus deposits were identified on HiRISE images. We mea-  
 94 sured the depths and thicknesses of identified layers on high-resolution topographic  
 95 data HiRISE digital terrain models (DTMs). We used two-origin HiRISE DTMs  
 96 1) produced by NASA/JPL/University of Arizona/USGS and 2) generated using  
 97 MarsSI (<https://marssi.univ-lyon1.fr/MarsSI/>), which includes processes us-  
 98 ing Ames Stereo Pipeline (*Quantin-Nataf et al.*, 2018). The procedure on MarsSI is  
 99 1) import HiRISE EDR images (raw data) and calibrate, 2) create DTMs, and 3)  
 100 align created DTMs to the MOLA data. Due to the availability of HiRISE DTMs,  
 101 we described stratigraphy at two points: point 1 and 2 (Fig.2). Since it is difficult  
 102 to describe facies in detail even in HiRISE images, we briefly classified layers into  
 103 three types by their appearance: fine, coarse, and very coarse. The fine layers have  
 104 no obvious boulders/rocks inside and correspond to the relatively weak layers shown  
 105 in *Beyer and McEwen* (2005). The very coarse layers look like fractured lava rock  
 106 or are boulder-rich. Some of them are described as the strong layers and interpreted  
 107 as the last basaltic lava flow by *Beyer and McEwen* (2005). Coarse layers have an  
 108 intermediate appearance between fine and very coarse layers. Based on this classifi-  
 109 cation, stratigraphic columns were created using StratGen (version 1.6.0) produced  
 110 by Indiana University, Indiana Geological Survey. We compared possible depths of  
 111 subsurface reflectors and those stratigraphies, then considered component materials  
 112 with plausible dielectric constant.

113 We identified subsurface reflectors on radargrams generated from radar sound-  
 114 ing data obtained by Mars SHallow RADar sounder (SHARAD) on Mars Recon-  
 115 naissance Orbiter (MRO) (*Seu et al.*, 2004). The operating frequency of SHARAD is  
 116 15 – 25 MHz, the bandwidth of which (10 MHz) corresponds to the vertical resolu-  
 117 tion of 8.4 m assuming pure water-ice (dielectric constant = 3.15) or 5.3 m for rock  
 118 with a dielectric constant = 8 (*Bramson et al.*, 2015). The spatial resolution, based  
 119 on synthetic aperture processing, is 0.3 to 1 km along the track direction and 3 to  
 120 7 km along the cross-track direction (*Seu et al.*, 2004). The MRO MARS SHARAD  
 121 5 RADARGRAM V1.0 we used was provided by the SHARAD team via the Geo-  
 122 sciences node of the Planetary Data System (PDS) at <http://pds-geosciences>

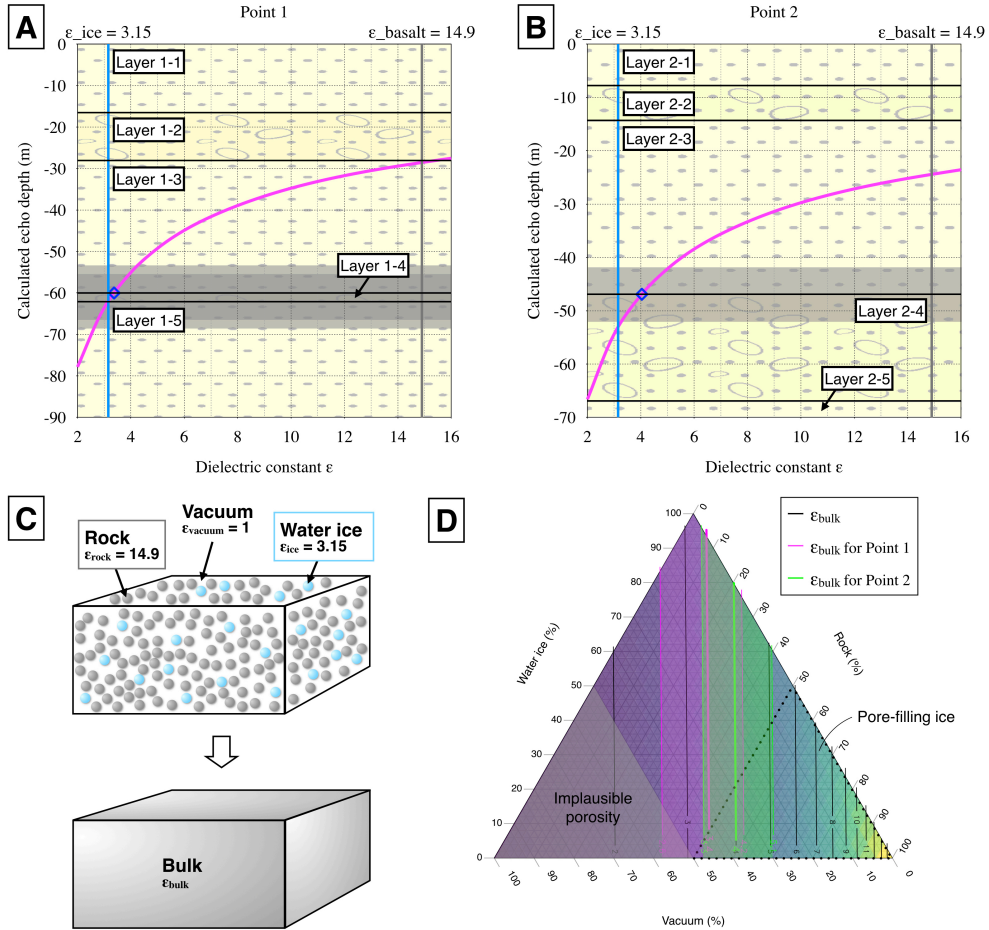


**Figure 1.** Estimation of dielectric constants (magenta lines) at point 1 (A) and 2 (B). Blue and gray lines indicate dielectric constant of water-ice and basalt, respectively. Depth of observed stratigraphy on HiRISE images is shown as black solid lines, and its  $\pm 5$  m error-margin is shown as gray rectangles. (C,D) Dielectric constant calculation based on *Ishiyama et al.* (2019). (C) The concept for bulk dielectric constant for a mixture of rock, air, and water-ice. (D) Ternary contour diagram of the bulk dielectric constant following the projection scheme of *Bramson et al.* (2015). A gray triangle zone indicates implausible porosities. Dotted triangle shows pore-filling ice condition.

123 .wustl.edu/missions/mro/sharad.htm. We analyzed 373 SHARAD radargrams  
 124 and identified subsurface reflectors (Fig.2).

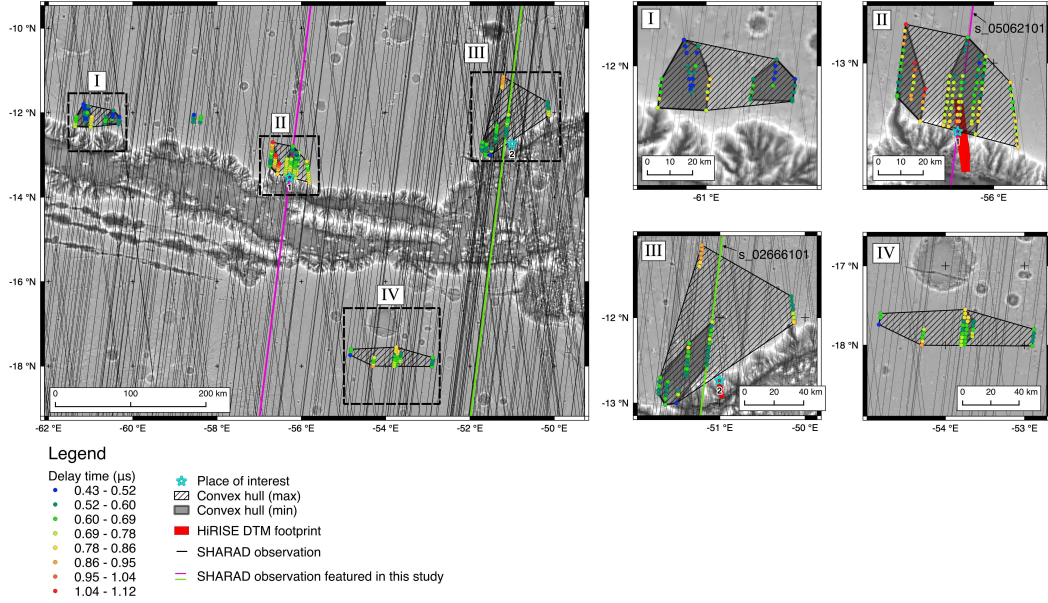


**Figure 2.** Investigated SHARAD observations (black, magenta, and green lines) and delay time of subsurface echoes (colored filled circles) in eastern Coprates and Capri Chasmata. Locations of the small maps on the right are shown in the larger left map (boxes with dashed outlines). Convex hulls of subsurface echo-identified points correlate to the calculation of coverage in Table 1. The base topographic map was created using HRSC MOLA Blended DEM (Ferguson *et al.*, 2018).

125 We should note that intense nadir and off-nadir surface echoes with their side-  
 126 lobes could overlap with weak subsurface echoes in the radargrams. Therefore, we  
 127 performed radar echo simulation by Kirchhoff Approximation Method, which calcu-  
 128 lates scattered electromagnetic fields at the Martian surface based on Mars Orbiter  
 129 Laser Altimeter (MOLA) data (Fig.S1B) and obtained simulated radargrams, in-  
 130 cluding surface echoes only. By comparing the observed and simulated radargrams,  
 131 we can identify subsurface echoes which are only found in observed radargrams. De-  
 132 tailed information for this simulation is shown in the supplementary information.  
 133 In addition, we checked if the levels of the identified subsurface echoes are more  
 134 than 10 dB higher than the sidelobe level of the nadir surface echoes. The sidelobe  
 135 level was estimated based on the Hann window, which is applied in the generation  
 136 of SHARAD data used in this study. Considering this calculation, subsurface re-  
 137 flectance was identified when the observed echo signal was 10 dB+ larger than the  
 138 calculated sidelobe (Fig.3D).

139 *Ishiyama et al.* (2019) gives the dielectric constant of a mixture of rocks, vac-  
 140 uum (air) and water-ice as

$$\epsilon_{bulk} = \epsilon_{vacuum} + \frac{3b}{1-b}\epsilon_{vacuum} \quad (1)$$

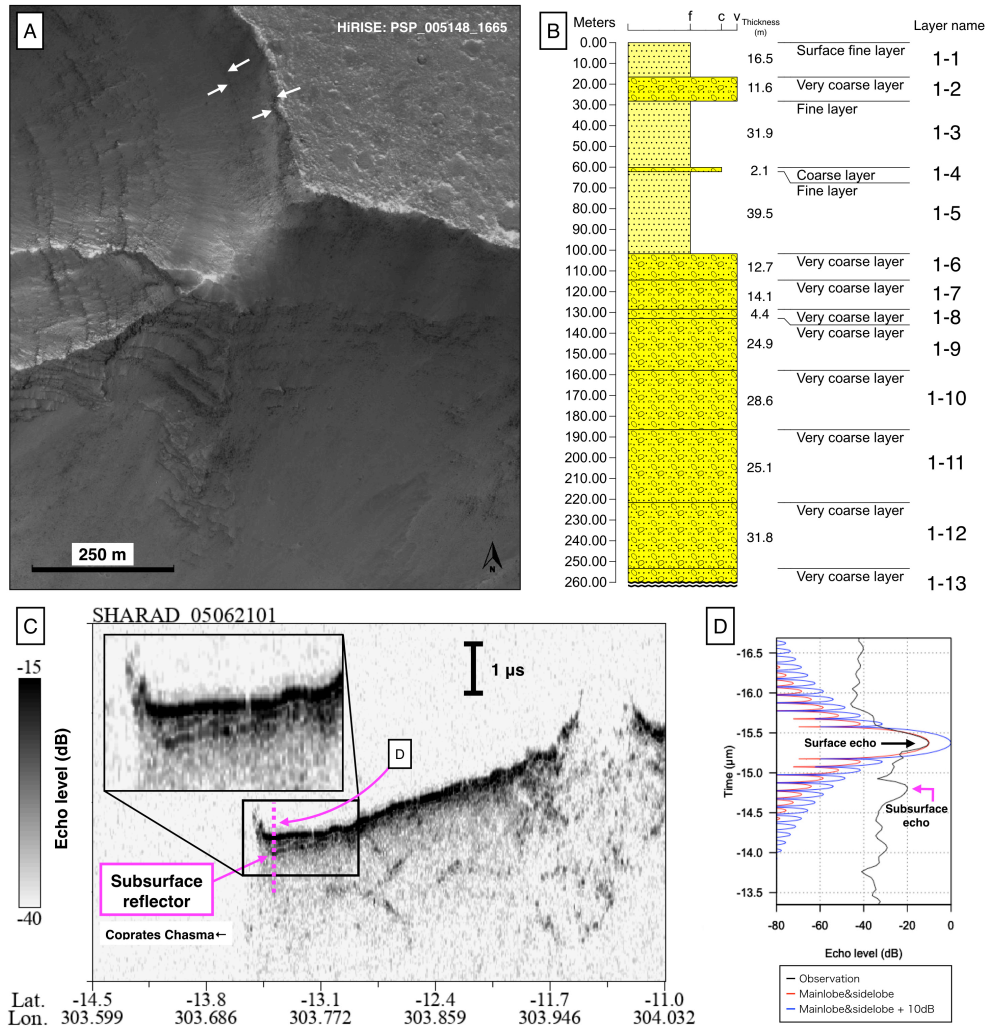


**Figure 3.** (A) Exposed stratigraphy on the wall, (B) its identified stratigraphy, and (C) its corresponding radargram at Point 1 in Fig.2. The thickness of each layer on the stratigraphic column (B) was measured on a HiRISE DTM (DTEED.014114.1665.005148.1665\_A01.IMG). (D) The echo level versus delay time (black line). Red and blue lines indicate sidelobe and sidelobe+10 dB.

$$b = \phi_{ice} \frac{\varepsilon_{ice} - \varepsilon_{vacuum}}{\varepsilon_{ice} + 2\varepsilon_{vacuum}} + \phi_{rock} \frac{\varepsilon_{rock} - \varepsilon_{vacuum}}{\varepsilon_{rock} + 2\varepsilon_{vacuum}} \quad (2)$$

141 where  $\varepsilon_{vacuum}$ ,  $\varepsilon_{rock}$ ,  $\varepsilon_{ice}$  are the dielectric constants of vacuum, rock and  
 142 water-ice (Fig.1C). Volume fractions of rock and ice in a target layer are shown as  
 143  $\phi_{rock}$  and  $\phi_{ice}$ . In the calculation, we applied  $\varepsilon_{vacuum} = 1$  and  $\varepsilon_{ice} = 3.15$  (pure  
 144 water-ice; *Matsuoka et al. (1997)*). Several previous studies applied a rock dielec-  
 145 tric constant around 8 (e.g., *Bramson et al., 2015*) though such low dielectric con-  
 146 stants are measured in non-porous dacite (e.g., 7.54 for Mount Meager - Ring Creek  
 147 dacite samples, *Rust et al. (1999)*). In this study, we applied  $\varepsilon_{rock} = 14.9$  (an av-  
 148 erage of 14.768 and 14.955 for Mauna Ulu basaltic lava basalt with no voids; *Rust*  
 149 *et al. (1999)*), since most of the observed rock on Mars has low-SiO<sub>2</sub> components,  
 150 which are comparable to basalt and andesite (*McSween et al., 2009*). Using these  
 151 equations and parameters, we estimated the plausible component materials in layers  
 152 above identified subsurface reflectors (Fig.1D).

153 From SHARAD observation data, we obtained the two-way delay time ( $\Delta t$ ) of  
 154 subsurface reflectors and calculated their depths ( $d$ ) by assigning a range of dielec-  
 155 tric constants ( $\varepsilon$ : 2 to 16) as

$$d = \frac{\Delta t \times c}{2} \times \frac{1}{\sqrt{\varepsilon_{bulk}}} \quad (3)$$

156 where  $c$  is the speed of light in a vacuum ( $3.0 \times 10^8$  m/s).

### 157 3 Results

158 We identified subsurface reflectors in four areas (I, II, III, and IV) of eastern  
 159 Coprates and northern Capri Chasmata (Fig.2). Areas I, II, and III are located at  
 160 the edge of the chasma plateau. Areas II and III are close to tiny tributary chas-  
 161 mata (Figs.2,S2). Area IV is located south of the Saravan crater. Though there are  
 162 many RSLs that have been found in eastern Coprates and Capri Chasmata (*Choj-*  
 163 *nacki et al., 2016; Stillman et al., 2017*), their distribution pattern is not correlated  
 164 with the subsurface reflector identified in this study. In this region, RSLs are lo-  
 165 cated on Nectaris Montes inside the chasmata; a difficult place to see subsurface  
 166 on SHARAD data due to its relatively small area and rough surface. The cover-  
 167 age of the four areas as concave hulls of subsurface reflector-identified places is  $0.3$   
 168  $- 1.1 \times 10^4$  km<sup>2</sup> in total and Table 1 shows the value for each one. The average delay  
 169 times of the subsurface echoes for these four areas is  $0.67 \mu\text{s}$  and those for each area  
 170 are shown in Table 1.

171 At point 1 in area II, we identified several stratigraphic layers (Fig.3A,B). The  
 172 uppermost fine layer (1-1) is 16.5 m thick, and the very coarse layer (1-2) has 11.6  
 173 m thickness. Beneath these layers, a 31.9 m thick fine layer (1-3) and a 2.1 m thick  
 174 very coarse subsurface layer (1-4) exist. Layer 1-4 corresponds to the strong layer  
 175 described by *Beyer and McEwen (2005)*. As noted in *Bramson et al., 2015*, shallow  
 176 reflectors within  $\sim 30$  m depth from the surface are obscured by sidelobes. There-  
 177 fore we regarded the delays of the subsurface echoes ( $0.73 \mu\text{s}$  in average of area II)  
 178 as representing bulk information of the dielectric constant above the reflectors (i.e.,  
 179 layers 1-1, 1-2, and 1-3). At point 1, the plausible bulk dielectric constant of the lay-  
 180 ers above the subsurface reflectors (delay time of the echoes from them:  $0.73 \mu\text{s}$ ),  
 181 which corresponds to the boundaries between the fine and coarse layers at a depth  
 182 of 60.0 m (bottom of layer 1-3 = top of layer 1-4), is estimated to be 3.4 (Fig.1A).  
 183 Regarding the error of reading for depth/thickness on a DTM as  $\pm 5$  m, the range of  
 184 plausible bulk dielectric constant is 2.6 to 4.2. Since the other remote sensing data

**Table 1.** Average two-way delay time of the subsurface echoes and coverage of the subsurface reflectors in each area. Area name corresponds to Fig.2. The coverage was calculated as a convex hull of the identified points in Fig.2.

| Area name | Average delay time ( $\mu\text{s}$ ) | Area ( $\text{km}^2$ ) <sup>1</sup> |
|-----------|--------------------------------------|-------------------------------------|
| I         | 0.58                                 | 782.5 – 1411.8                      |
| II        | 0.73                                 | 846.4 – 1998.5                      |
| III       | 0.66                                 | 925.1 – 5259.0                      |
| IV        | 0.67                                 | 153.2 – 2251.5                      |
| Total     |                                      | 2707.2 – 10920.7                    |

<sup>1</sup> Minimum: only for main clusters of subsurface echo-identified points in shadow convex hulls of Fig.2. Maximum: for whole subsurface echo-identified points in hatched convex hulls of Fig.2

185 such as HiRISE color images and CRISM absorptions does not show strong features  
 186 for water-ice on the chasma wall, layers 1-1, 1-2, and 1-3 are believed to be a pore-  
 187 filling ice regime, not an excess ice regime (*Bramson et al.*, 2015). Assuming that  
 188 these layers are pore-filling ice regime, the value of the calculated dielectric constant  
 189 ( $\sim 3.4$ ) is consistent with a rock-air mixture with 46.1 % porosity and a rock-air-ice  
 190 mixture, for which the range of volume fraction of water-ice is 0 – 7.8 % (Fig.1D).

191 At point 2 in area III, the uppermost fine layer (2-1) has 7.8 m thickness, and  
 192 the very coarse subsurface layer (2-2) has 6.6 m thickness (Fig.S2). Beneath these  
 193 layers, a 32.6 m thick fine layer (2-3) and 20.0 m thick very coarse layer (2-4) exist.  
 194 Layer 2-4 corresponds to the strong layer described by *Beyer and McEwen* (2005).  
 195 The bulk dielectric constant of the layers above the subsurface reflectors (average de-  
 196 lay time in area III: 0.66  $\mu\text{s}$ ), which corresponds to the boundary between the fine  
 197 and coarse layers at a depth of 46.9 m (bottom of layer 2-3 = top of layer 2-4), is es-  
 198 timated to be 4.0 (range of 3.3 to 5.1, considering the error of depth/thickness read-  
 199 ing)(Fig.1B). This value is consistent with 39.3 % porosity for the rock-air mixture  
 200 and up to 21.2 % of the volume fraction of ice for the rock-air-ice mixture (Fig.1D).

## 201 4 Discussion and conclusion

202 From the analysis of radar sounding data, high-resolution images and topo-  
 203 graphic data, we found that eastern Coprates and Capri Chasmata have areas with  
 204 relatively low dielectric constants. The calculated bulk dielectric constant (3.4–4.0)  
 205 suggests that the layers are composed of a rock-air mixture with up to  $\sim 46.1$  %  
 206 porosity and a rock-ice-air mixture with up to  $\sim 21.2$  % volume fraction of water-  
 207 ice. In the equatorial region, it has been estimated that water-ice is unstable due  
 208 to the sublimation and thus a cryosphere does not currently exist (*Schorghofer and*  
 209 *Aharonson*, 2005). Considering the instability of ice, the layers with low bulk dielec-  
 210 tric constant should be a porous rock layer without water-ice. It is certainly true  
 211 that  $\sim 46$  % of the calculated porosity in this study is possible for general geologic  
 212 materials such as those of aeolian, fluvial, and volcanic origins (*Todd and Mays*,  
 213 2005), which possibly exist in eastern Coprates and Capri Chasmata. However, or-  
 214 bital simulations have suggested that the obliquity of Mars oscillates periodically. In  
 215 this case, water could be transported to the low-latitude region at the high obliquity  
 216 stage. *Head et al.* (2003) evaluates that the last high obliquity stage occurred  $\sim 0.4$   
 217 Myr ago. *Bryson et al.* (2008) performed the experiments on the sublimation rate  
 218 of water-ice beneath regolith, and their conclusion suggests that  $\sim 1$  m-thick water-

219 ice can be maintained for 0.4 Myr under  $\sim 2$  m-thick regolith. Although the age of  
 220 the low dielectric constant layer is uncertain, if ice was deposited in the layer  $\sim 0.4$   
 221 Myr ago, the existence of water-ice at the depth in which the reflector was identified  
 222 ( $\sim 60$  m) cannot be ruled out. From crater counting, the age of water-ice detected  
 223 by radar sounding in the mid-latitude area is evaluated to be  $\sim 20$  Myr (*Viola et*  
 224 *al.*, 2015). Thus, if the layers in the equatorial area contain water-ice, the time when  
 225 water-ice was deposited should differ between mid-latitude and low-latitude regions.  
 226 In addition to the preservation of water-ice at a time of high-obliquity, the accumu-  
 227 lation of water-ice in the pores by thermal contraction is also suggested (*Fisher,*  
 228 2005), which may be the another origin of pore water-ice in eastern Coprates and  
 229 Capri Chasmata.

230 If the layer is composed of a rock-ice-air mixture, using the estimated water-  
 231 ice volume fraction in a layer of a specific thickness, the possible amount of water-  
 232 ice can be calculated. In area II, assuming a layer  $846.4$  to  $1998.5$  km<sup>2</sup> that is  $60.0$   
 233 m thick with  $7.8$  % volume fraction of water-ice,  $4.0$  to  $9.4$  km<sup>3</sup> of putative water-  
 234 ice would exist. However, considering the emplacement of water-ice in  $0.4$  Ma by  
 235 snowfall (e.g., *Christensen*, 2003), it is natural to think a host layer of water-ice is  
 236 located above the strong layer, which is described as a Hesperian lava flow (*Witbeck*  
 237 *et al.*, 1991). This stratigraphic setting (water-ice can exist in the topmost layer)  
 238 leads to the volume fraction of putative water-ice in the topmost layer being  $29$  %.  
 239 This calculation can be applied to  $925$  to  $5258$  km<sup>2</sup> of the subsurface reflectors re-  
 240 gion in area III. Based on the analysis of radar sounding data, in point 2 in area  
 241 III, the plausible water-ice volume fraction of a  $46.9$  m thick layer is  $21.2$  %. Al-  
 242 though this condition simply leads to a volume range of putative water-ice from  $9.2$   
 243 to  $52.4$  km<sup>3</sup>, the volume of putative water-ice in area III would be less than  $7.2$  km<sup>3</sup>  
 244 assuming a pore-filling water-ice regime (less than  $50$  % water-ice content) in the  
 245  $5259.0$  km<sup>2</sup>-extent of a  $7.8$  m-thick topmost layer. Therefore, a maximum of  $16.6$   
 246 km<sup>3</sup> of putative water-ice may exist in the plateau of eastern Coprates and northern  
 247 Capri Chasmata. On the gamma-ray spectrum, eastern Coprates and Capri Chas-  
 248 mata do not show a strong hydrogen concentration (*Boynton et al.*, 2007). Since  
 249 the detection depth of the hydrogen is approximately  $1$  m (*Feldman et al.*, 2004),  
 250 the water-ice layers in these regions are thought to be undetectable by the gamma-  
 251 ray spectrum. The surface echo power analyses of radar sounding data by the Mars  
 252 Advanced Radar for Subsurface and Ionospheric Sounding instrument (MARSIS)  
 253 showed the dielectric constant property at a few decameters below the surface (*Moug-*  
 254 *inot et al.*, 2010). On their dielectric map, dielectric constants in eastern Coprates  
 255 and Capri Chasmata decrease from southwest to northeast. This suggests drastic  
 256 variation in the shallow subsurface environment, such as from dry to ice-rich or the  
 257 increase of porosity in these areas. Thus, although deducing accumulation mecha-  
 258 nisms is still challenging, our analyses imply the possible existence of a subsurface  
 259 ice-contained layer in eastern Coprates and northern Capri Chasmata, i.e., even in  
 260 the equatorial region.

261 In this work, from the bulk dielectric constant evaluated from the delay time of  
 262 radar sounding and plausible corresponding depth at the stratigraphic exposure, we  
 263 could only constrain the upper limit of the water-ice fraction. Thus, considering the  
 264 current instability of water-ice in low-latitude terrain, further studies and discussions  
 265 are required to determine the existence of water-ice and, if water-ice actually exists,  
 266 for the mechanism to maintain it within low-latitude terrain.

## 267 Acknowledgments

268 We used the data of SHARAD and HiRISE on the Planetary Data System and the  
 269 website of the University of Arizona (<https://hirise.lpl.arizona.edu/>). HiRISE  
 270 DTMs have been processed with the MarsSI (<https://marssi.univ-lyon1.fr/>)

271 MarsSI/) application with the support of Matthieu Volat. Discussion with Isaac B  
 272 Smith greatly improved our analysis. We appreciate Lucy Kwok for the generous  
 273 effort of editing the English in this manuscript. We also thank J. L. Whitten and  
 274 an anonymous reviewer for their thorough reviews. This work was supported by the  
 275 JSPS Grants-in-Aid for Scientific Research (KAKENHI 17H06459 and 19H00707).

## 276 References

- 277 Beyer, R.A. and A.S. McEwen, 2005, Layering stratigraphy of eastern Coprates and  
 278 northern Capri Chasmata, Mars, *Icarus*, **179**(1), 1–23.
- 279 Boynton, W.V., et al., 2007, Concentration of H, Si, Cl, K, Fe, and Th in the low-  
 280 and mid- latitude regions of Mars, *J. Geophys. Res.*, **112** E12.
- 281 Bramson, A.M., S. Byrne, N.E. Putzig, S. Sutton, J.J. Plaut, T.C. Brothers, and  
 282 J.W. Holt, 2015, Widespread excess ice in Arcadia Planitia, Mars, *Geophys.*  
 283 *Res. Lett.*, **42**(16), 6566–6574.
- 284 Bryson, K.L., V. Chevrier, D.W. Sears, and R. Ulrich, 2008, Stability of ice on Mars  
 285 and the water vapor diurnal cycle: Experimental study of the sublimation of  
 286 ice through a fine-grained basaltic regolith, *Icarus*, **196**(2), 446–458.
- 287 Byrne, S., C.N. Dundas, M.R. Kennedy, M.T. Mellon, A.S. McEwen, S.C. Cull et  
 288 al., 2009, Distribution of mid-latitude ground ice on Mars from new impact  
 289 craters, *Science*, 325.5948: 1674–1676.
- 290 Carr, M.H., and J.W. Head, 2010, Geologic history of Mars, *Earth and Planet. Sci.*  
 291 *Lett.*, **294**, 185–203, doi:10.1016/j.epsl.2009.06.042.
- 292 Chojnacki, M., and B.M. Hynek, 2008, Geological context of water- altered minerals  
 293 in Valles Marineris, Mars, *J. Geophys. Res.*, **113** E12.
- 294 Chojnacki, M., A. McEwen, C. Dundas, L. Ojha, A. Urso, and S. Sutton, 2016, Geo-  
 295 logic context of recurring slope lineae in Melas and Coprates Chasmata, Mars,  
 296 *J. Geophys. Res.*, **121**(7), 1204–1231.
- 297 Christensen, P.R., 2003, Formation of recent Martian gullies through melting of ex-  
 298 tensive water-rich snow deposits, *Nature*, 422(6927), 45.
- 299 Clifford, S.M., J. Lasue, E. Heggy, J. Boisson, P. McGovern, and M.D. Max, 2010,  
 300 Depth of the Martian cryosphere: Revised estimates and implications for the  
 301 existence and detection of subpermafrost groundwater, *J. Geophys. Res.*, **115**,  
 302 E7.
- 303 Dundas, C.M., S. Byrne, A.S. McEwen, M.T. Mellon, M.R. Kennedy, I.J. Daubar,  
 304 and L. Saper, 2014, HiRISE observations of new impact craters exposing Mar-  
 305 tian ground ice, *J. Geophys. Res.*, **119**(1), 109–127.
- 306 Dundas, C.M., A.S. McEwen, M. Chojnacki et al., 2017, Granular flows at recurring  
 307 slope lineae on Mars indicate a limited role for liquid water, *Nature Geosci.*,  
 308 **10**, 903–907, doi:10.1038/s41561-017-0012-5.
- 309 Dundas, C.M. et al., 2018, Exposed subsurface ice sheets in the Martian mid-  
 310 latitudes, *Science*, 359.6372: 199–201.
- 311 Feldman, W.C. et al., 2004, Global distribution of near- surface hydrogen on Mars,  
 312 *J. Geophys. Res.*, **109**(E9).
- 313 Ferguson, R.L, Hare, T.M., Laura, J., 2018, HRSC and MOLA Blended Digital El-  
 314 evation Model at 200m v2, Astrogeology PDS Annex, U.S. Geological Survey,  
 315 URL: [http://bit.ly/HRSC\\_MOLA\\_Blend\\_v0](http://bit.ly/HRSC_MOLA_Blend_v0)
- 316 Fisher, D.A., 2005, A process to make massive ice in the martian regolith using long-  
 317 term diffusion and thermal cracking, *Icarus*, **179**(2), 387–397.
- 318 Head, J.W. and D.R. Marchant, 2003, Cold-based mountain glaciers on Mars: west-  
 319 ern Arsia Mons, *Geology*, 31(7), 641–644.
- 320 Head, J.W., J.F. Mustard, M.A. Kreslavsky, R.E. Milliken, and D.R. Marchant,  
 321 2003, Recent ice ages on Mars, *Nature*, 426(6968), 797.
- 322 Ishiyama, K., A. Kumamoto, Y. Takagi, N. Nakamura, and S. Hasegawa, 2019, Ef-  
 323 fect of crack direction around laboratory-scale craters on material bulk permit-

- 324 tivity, *Icarus*, **319**, 512–524.
- 325 Matsuoka, T., S. Fujita, and S. Mae, 1997, Dielectric properties of ice containing  
326 ionic impurities at microwave frequencies, *J. Phys. Chem. B*, **101**(32), 6219–  
327 6222.
- 328 McSween, H.Y., G.J. Taylor, and M.B. Wyatt, 2009, Elemental composition of the  
329 Martian crust, *Science*, **324**(5928), 736–739.
- 330 Milkovich, S.M., J.W. Head, and D.R. Marchant, 2006, Debris-covered piedmont  
331 glaciers along the northwest flank of the Olympus Mons scarp: Evidence for  
332 low-latitude ice accumulation during the Late Amazonian of Mars, *Icarus*,  
333 **181**(2), 388–407.
- 334 Mellon, M. T., et al., 2009, Ground ice at the Phoenix Landing Site: Stability state  
335 and origin, *J. Geophys. Res.*, **114**, E00E07, doi:10.1029/2009JE003417.
- 336 Morgan, G.A. et al., 2019, The Mars Subsurface water-ice Mapping (SWIM)  
337 Project, paper presented at the 50th Lunar and Planetary Science Conference,  
338 Lunar and Planetary Institute, The Woodlands, Tex.
- 339 Mouginot, J. et al., 2010, The 3–5 MHz global reflectivity map of Mars by MAR-  
340 SIS/Mars Express: Implications for the current inventory of subsurface H<sub>2</sub>O,  
341 *Icarus*, **210**(2), 612–625.
- 342 Orosei, R. et al., 2018, Radar evidence of subglacial liquid water on Mars, *Science*,  
343 **361**(6401), 490–493.
- 344 Putzig, N.E., I.B. Smith, M.R. Perry, F.J. Foss II, B.A. Campbell, R.J. Phillips, and  
345 R. Seu, 2018, Three-dimensional radar imaging of structures and craters in the  
346 Martian polar caps, *Icarus*, **308**, 138–147.
- 347 Quantin-Nataf, C. et al., 2018, MarsSI: Martian surface data processing information  
348 system, *Planetary and Space Science*, **150**, 157–170.
- 349 Rust, A.C., J.K. Russell, and R.J. Knight, 1999, Dielectric constant as a predictor of  
350 porosity in dry volcanic rocks, *J. Volcanol. Geotherm. Res.*, **91**(1), 79–96.
- 351 Seu, R. et al., 2004, SHARAD: The MRO 2005 shallow radar, *Planetary and Space  
352 Science*, **52**(1-3), 157–166.
- 353 Smith, I.B., C. Viviano, M. Chojnacki, N.E. Putzig, C. Quantin, and J.A.P. Ro-  
354 driguez, 2019, Characterization of Hydrated, Layered Deposits at Valles  
355 Marineris Plateau, a Multidisciplinary Approach, paper presented at the 50th  
356 Lunar and Planetary Science Conference, Lunar and Planetary Institute, The  
357 Woodlands, Tex.
- 358 Stillman, D.E., T.I. Michaels, and R.E. Grimm, 2017, Characteristics of the numer-  
359 ous and widespread recurring slope lineae (RSL) in Valles Marineris, Mars,  
360 *Icarus*, **285**, 195–210.
- 361 Schorghofer, N., and O. Aharonson, 2005, Stability and exchange of subsurface ice  
362 on Mars, *J. Geophys. Res.*, **110**, E5.
- 363 Stuurman, C.M., G.R. Osinski, J.W. Holt, J.S. Levy, T.C. Brothers, M. Kerrigan,  
364 and B.A. Campbell, 2016, SHARAD detection and characterization of sub-  
365 surface water ice deposits in Utopia Planitia, Mars, *Geophys. Res. Lett.*, **43**,  
366 9484–9491, doi:10.1002/2016GL070138.
- 367 Todd, D.K. and L.W. Mays, 2005, Groundwater hydrology, 3rd ed, pp 636.
- 368 Touma, J., and J. Wisdom, 1993, The chaotic obliquity of Mars, *Science*, **259**(5099),  
369 1294–1297.
- 370 Viola, D., A.S. McEwen, C.M. Dundas, and S. Byrne, 2015, Expanded secondary  
371 craters in the Arcadia Planitia region, Mars: Evidence for tens of Myr-old  
372 shallow subsurface ice. *Icarus*, **248**, 190–204.
- 373 Witbeck, N.E., K.L. Tanaka, and D.H. Scott, 1991, Geologic map of the Valles  
374 Marineris region, Mars, No. MAP I-2010, US Geological Survey Report.